CHALMERS
UNIVERSITY OF TECHNOLOGY

High temperature oxidation of inconel 939 produced by additive manufacturing

Downloaded from: https://research.chalmers.se, 2024-05-11 19:42 UTC

Citation for the original published paper (version of record):
Visibile, A., Gündüz, K., Sattari, M. et al (2024). High temperature oxidation of inconel 939 produced by additive manufacturing. Corrosion Science, 233.
http://dx.doi.org/10.1016/j.corsci.2024.112067

N.B. When citing this work, cite the original published paper.

research.chalmers.se offers the possibility of retrieving research publications produced at Chalmers University of Technology.
It covers all kind of research output: articles, dissertations, conference papers, reports etc. since 2004.
research.chalmers.se is administrated and maintained by Chalmers Library

(article starts on next page)

Corrosion Science 233 (2024) 112067

Contents lists available at ScienceDirect

Corrosion Science

journal homepage: www.elsevier.com/locate/corsci

High temperature oxidation of inconel 939 produced by additive manufacturing

Alberto Visibile [a,1], Kerem Ozgur Gunduz [a,b,1], Mohammad Sattari [c], Irina Fedorova [c,d], Mats Halvarsson [c], Jan Froitzheim [a,*]

[a] Chalmers University of Technology, Department of Chemistry and Chemical Engineering, Kemivägen 10, Gothenburg SE-412 96, Sweden
[b] Gebze Technical University, Department of Materials Science and Engineering, Gebze, Kocaeli 41400, Turkey
[c] Chalmers University of Technology, Department of Physics, Division of Microstructure Physics, Gothenburg SE-412 96, Sweden
[d] Kanthal AB, Division of Research and Development, Sörkvarnsvägen 3, Hallstahammar SE-73427, Sweden

ARTICLE INFO

Keywords:
Additive manufacturing
Laser-Powder Bed Fusion
IN939
High temperature oxidation
Cr_2O_3
Spallation

ABSTRACT

High temperature oxidation of additively manufactured (Laser-powder bed fusion) IN939 (AM IN939) was studied at 900°C in dry air for 168 hours. AM IN939 cut parallel/perpendicular to the building direction, including conventionally manufactured (CM) IN939 were exposed to assess the influence of AM microstructure and its inherent anisotropy on oxidation properties. Microstructural anisotropy had no significant impact on oxidation properties. AM and CM IN939 exhibited nearly identical mass gains, yet local spallation was observed in the former. Further investigation involved oxidation of heat-treated AM IN939, revealing improved adhesion, possibly due to transformation of fine dendritic/cellular structure into coarse equiaxed grains.

1. Introduction

Nickel-based superalloys are corrosion-resistant alloys that are specially designed for high-temperature applications up to 1100–1150°C [1–3]. Due to their high levels of resistance to creep, sulfidation, and oxidation, these alloys have been widely used in the aerospace and energy industries since the 1950s. They usually contain up to 10 alloying elements, including light elements, such as carbon or boron, and heavy refractory elements such as Ta, W, Nb or Re [4–6].

Inconel 939 (IN939; also known as Nimocast 739), which is a high-chromium-content superalloy developed by Inco Europe Ltd., is commonly used in turbine blades and vanes [7–9]. This alloy has good weldability and adequate strength (γ' former) at operating temperatures of up to 950°C [10,11]. IN939 and similar superalloys, such as IN718, IN625 and René 220, form Cr_2O_3 scales through the preferential oxidation of Cr, which protects the metal against high temperature corrosion. The formed chromia layer is usually dense and slow-growing, obeying the parabolic rate law and exhibiting a long service lifetime at operating temperatures of up to 1000°C. When in service, the Cr_2O_3 layer is subjected to stresses, especially under cyclic conditions, which may result in the spallation of this layer. The spalled regions can be healed by re-formation of the Cr_2O_3 layer, if the alloy can supply sufficient Cr to the surface of the alloy.

For many applications, in particular for turbines, highly complex geometries, such as internal cooling ducts, are required [12]. In this context, conventional casting techniques have certain limitations, as the geometry of the final product is restricted by the shape of the mold in which the molten metal is cast into. Therefore, secondary techniques such as machining and welding are required, albeit they are time-consuming and increase the cost. For this reason, additive manufacturing techniques have great potential for the development of products that have highly complex geometries, as they enable increased freedom of design compared to conventional casting techniques. Additive manufacturing allows the production of 3D objects with unconventional or complex designs through layer-upon-layer deposition of material following a 3D computer design, also referred as 3D printing [13–15].

However, the microstructures of additively manufactured (AM) materials are significantly different from those of conventionally manufactured (CM) materials. It is well-known that the heat flux during the process strongly influences the microstructures of the AM materials, resulting in defined highly anisotropic microstructural features [16–23].

* Corresponding author.
E-mail address: jan.froitzheim@chalmers.se (J. Froitzheim).
[1] Both of these authors equally contributed to this work.

https://doi.org/10.1016/j.corsci.2024.112067
Received 14 November 2023; Received in revised form 4 April 2024; Accepted 17 April 2024
Available online 18 April 2024
0010-938X/© 2024 The Author(s). Published by Elsevier Ltd. This is an open access article under the CC BY license (http://creativecommons.org/licenses/by/4.0/).

For example, the variation of material's mechanical properties perpendicular and parallel to building direction has been reported in several studies on AM materials, such as IN625 and IN718 [24–27]. For instance, in a study by Condruz et al. [28] the effect of three different scanning angles (90°, 67°, 45°) coupled with four different building directions (Z, X, Y axis and 45° tilt on ZX plane) on the mechanical properties of AM IN625 were studied. In all different scanning strategies, samples grown on Z-axis exhibited the weakest mechanical properties. UTS for the Z-axis was approximately 800 MPa in all cases while other directions were in the range of 850–1000 MPa [28].

The mechanical properties of AM IN939 were investigated by several studies [29–35]. These studies have mainly focused on improving the mechanical and thermal properties of AM IN939 by optimizing the printing parameters and heat treatment procedures. Nevertheless, only a few studies have been published that have evaluated the effects of the AM microstructure on the high-temperature oxidation behaviors of Cr_2O_3-forming Ni-based alloys, mainly concentrating on IN718 and IN625 [36–42]. From these previous studies, on IN625 and IN718 it has been concluded that: 1) microstructural anisotropy has no effect on the oxidation properties; 2) the oxidation rates of AM materials are slightly higher than those of CM materials; and 3) severe intergranular oxidation exists in AM materials (IN625 and IN718). A recent study has shown that in IN625 severe intergranular oxidation is not due to the AM microstructure but rather occurs due to minor differences in chemical composition, as proven by careful heat treatments and thermomechanical processing of as-built material [42,43].

However, the high temperature oxidation behavior of AM γ' strengthened Ni-base superalloys is studied to a far lesser extent [44,45].

Kim et al. [44] studied the high temperature oxidation behavior of AM IN738LC in as-built and heat-treated (solution treatment + aging) condition. As-built samples were oxidized between 1073 and 1373 K while for comparison purposes, as-built and heat-treated AM IN738LC were exposed at 1273 and 1373 K. At 1273 K, mass gain vs time curves of as-built and heat-treated material are almost identical and showed no significant difference. However, at 1373 K heat-treated IN738LC showed better performance compared to as-built IN738LC. At 1373 K, as-built IN738LC only formed Cr_2O_3 as a protective scale while heat-treated IN738LC formed Cr_2O_3 on γ and fine γ' regions but Al_2O_3 scales on primary γ' regions which resulted in lower mass gains [44].

In another study, AM 14 Ni-base alloys (novel compositions and industrially available compositions) including IN939 are oxidized at 1000 °C for 24 h in isothermal conditions [45]. On IN939, porous Cr_2O_3 scales decorated with Cr_2TiO_5 and TiO_2 precipitates on the gas oxide interface were observed. Despite being porous, Cr_2O_3 scales on AM IN939 were rather uniform in thickness. Additionally, an internal oxidation zone (IOZ) composed of $NiAl_2O_4$ and Al_2O_3 were found in the subscale region followed by TiN precipitates forming an internal nitridation zone (INZ) towards the metal [45].

Although this study provides valuable initial information on the high-temperature oxidation of AM IN939, a more-detailed investigation is required to elucidate the oxidation behavior of AM IN939 by comparing AM and CM materials especially on service temperatures where IN939 alloy is commonly utilized. This comparison would also determine whether AM IN939 can replace CM IN939 in terms of high-temperature oxidation properties.

This work compares AM IN939 and CM IN939 exposed under the same oxidizing conditions (900°C, dry air) for a specific amount of time (168 h). A detailed study of the oxide scales of the AM and CM materials is carried out using mass gain measurements, x-ray diffraction (XRD), and microstructural investigations with scanning electron microscopy (SEM) and energy dispersive x-ray spectroscopy (EDX), both before and after the exposure.

2. Experimental

IN939 alloys produced by AM (Laser-Powder Bed Fusion, L-PBF) and by CM using casting were provided by Siemens Industrial Turbomachinery AB (Finspång, Sweden). Hereinafter, the L-PBF-produced IN939 will be referred to as AM IN939, while the standard material produced by casting will be referred to as CM IN939. The chemical compositions of the alloys are given in Table 1. For AM IN939, except for carbon (C), nitrogen (N) and oxygen (O) measurements, the analyses were carried out using inductively coupled plasma-mass spectrometry (ICP-MS). The chemical composition of CM was determined with spark optical emission spectrometry (Spark-OES). The concentration of C, N and O for both alloys were determined by combustion infrared absorption method.

The CM IN939, used as a reference, was produced by the investment casting method and was provided as a rod with the diameter of 20 mm. The AM IN939 alloy was provided as metal cubes with 20 mm per side in as-printed conditions. The CM IN939 (grain size, 100–300 μm) rod and the AM IN939 cubes were then cut into thinner slices using electrical discharge machining (EDM). The AM material was cut along different directions: AM-Z (the cutting plane was normal to the building direction), as well as AM-X and AM-Y, which were perpendicular to each other and parallel to the building direction. The microstructures of AM-X and AM-Y were found to be similar, and are hereinafter referred to as AM-Y. After sectioning the samples, the largest surfaces were polished with a 1-μm diamond suspension as the final step, while the edges of the samples were ground with SiC emery paper up to 4000 grit. Samples for electron backscatter diffraction (EBSD) analysis were further polished with a 0.25-μm diamond suspension and subsequently with colloidal silica (≈50 nm). After polishing, each specimen was rinsed initially with deionized water, and then placed in an ultrasonic bath with acetone and ethanol for 10 minutes each. To evaluate the microstructures of the samples before exposure, one sample of each material and cut section was electrochemically etched in 0.1 $g \cdot ml^{-1}$ oxalic acid solution, to reveal the microstructure (etching parameter: 5 V for 10 seconds). Optical microscopy images of etched AM IN939 were captured by Nikon Eclipse E100 optical microscope. Regarding the AM IN939 unexposed samples, EBSD was performed to determine the dominant orientation and shape/size of the grains for the AM-Z and AM-Y samples using a ZEISS Ultra 55 SEM equipped with the Nordlys EBSD detector. The mass gain after 168 h was measured using a Mettler Toledo XP6 microbalance with 0.1-μg resolution.

As-printed AM IN939 samples were heat-treated in an evacuated sealed quartz tube with a volume of circa 10 ml. The samples were solution-treated for 1 week at 1160°C, and subsequently subjected to an aging step of 24 hours at 800°C. This procedure was chosen to mimic the two step heat-treatment commonly employed on IN939 vanes [46,47] The very thin layer of oxide formed under this condition was removed with sandpaper, grinding off at least 0.3 mm of material from each material surface. The same surface preparation procedure was followed as for the heat-treated material.

The exposures were performed isothermally in tube furnaces at 900°C with a 1.1 cm/sec flow velocity for 168 h in filtered laboratory air. The exposures were carried out in dry air. To determine the exact temperature and detect the hottest spot in the furnace, an external S-type thermocouple was used to profile the temperature. The samples were placed in the hottest zone, where the temperature deviated by ±3°C within 5 cm. At least two exposures were made for each sample type, to ensure that the results were reproducible.

A Siemens D5000 x-ray diffractometer (Cu Kα radiation) was employed to perform grazing incidence x-ray diffraction (GI-XRD) analysis on samples after exposure. A grazing incidence angle of 0.5–2.0° was used, and a 2θ range of 20°–80° was measured with a step size of 0.05°. SEM analysis was performed using an FEI ESEM Quanta 200 equipped with an Oxford X-MAX 80 EDX detector. Images were captured with secondary electron (SE) and backscattered electron (BSE) detectors.

Cross-sections of the exposed samples were prepared by cutting the samples in half with a low-speed saw and subsequently milling them with the Leica TIC3X broad ion beam (BIB) instrument (3 mA, 8 kV, 5 h).

Table 1
Alloy compositions for AM IN939 and CM IN939 (in wt%). N and O are given in PPM (mass).

	Cr	Co	W	Nb	Ti	Al	Ta	Mo	Zr	Fe	Si	C	N	O	Ni
CM	22.9	19.9	1.8	0.9	3.4	2.0	1.11	0.03	0.07	<0.1	0.04	0.13	43	40	Bal.
AM	22.1	18.6	2.0	1.0	3.6	2.0	1.59	0.03	0.03	0.3	<0.1	0.13	81	106	Bal.

This preparation method avoids crack formation/spallation in the cross-section, which usually occurs during the classical metallographic method of sample preparation [48].

3. Results and Discussion

Fig. 1 shows optical micrographs of the etched microstructures (Fig. 1, A and B) and the EBSD inverse pole figure (IPF) maps (Fig. 1, C and D) of AM IN939 oriented parallel and perpendicular to the building direction. The etched images of the samples prepared parallel to the building direction (AM-Y) reveal melt pools with an average size of 100–120 μm (Fig. 1A). IPF maps of the AM-Y sample further reveal that the material is composed of discontinuous elongated grains of approximately 60–80 μm in size (width of columns), while smaller columns of about 10 μm in width are also present. The IPF maps also show that these columns are mostly oriented in <001> direction, while some of them are also oriented in the <110> direction and, seldomly, in the <111> direction. Interestingly, the melt pool lines do not interrupt the orientations of the columnar grains. In the literature, this behavior is explained by epitaxial nucleation and the growth of newly formed grains on previously formed columnar or dendritic grains, thereby preserving the same orientation [49–51].

In Fig. 1B, the AM-Z IN939 exhibits a peculiar microstructure, with elongated grains in two directions that are perpendicular to each other, which has previously been described as the basket-weave microstructure [52]. According to the IPF map of AM-Z, the repeating units are approximately 60–80 μm long and 15–35 μm wide. They are separated by 10–15 μm-wide areas of small grains with apparently random orientation. Thus, the units can be considered as rectangles with a high aspect ratio (length:width ratio). The distance between the boundaries (length) most probably corresponds to the hatch distance. However, local disturbances of this pattern are found in IPF maps, as indicated by the black rectangle in Fig. 1D. Furthermore, the grains are mostly oriented in the <001> direction, although some of them are also oriented in the <110> and <111> directions, as observed for AM-Y. This microstructure occurs as a result of the scanning strategy and processing parameters, since in each step, the direction of the laser track changes and forms repeating units perpendicular to the building direction and a columnar structure parallel to the building direction. Similar microstructures have also been identified in previous works [53].

SEM-BSE images of the unexposed CM IN939 and AM IN939 samples are shown in Fig. 2. They reveal some differences in the microstructures of these alloys. AM-Y in Fig. 1A shows melt pools separated by melt pool boundaries. In addition, the high-magnification image in the inset to Fig. 2, reveals a dendritic/cellular substructure with 1-μm in size as well as the presence of very small precipitates (bright particles of diameter <100 nm) distributed throughout the microstructure. As expected, γ' precipitates were absent in the as-printed microstructure due to the rapid cooling during the solidification process [32,54,55]. Compared to dendrites or cell cores, interdendritic/intercellular regions appear brighter, indicating segregation of heavy metals into those regions, as observed in previous studies [56,57]. The bright precipitates resemble the MC carbides observed by Shaikh et al. [58] and Tang et al. [55]. Unfortunately, these bright particles are too small to be analyzed by classical SEM-EDX investigations; more-dedicated studies with TEM are needed. In the CM IN939 samples, large precipitates are visible, mainly composed of Ta, Nb and Ti according to the SEM-EDX mapping analysis (Fig. S1). Earlier works have shown that IN939 possesses relatively large blocky carbides, with dimensions of a few micrometers and with the formula (Ta, Nb, Ti, W)C and these carbides oxidize faster than the matrix [47]. Therefore, the precipitates observed in CM IN939 in Fig. 2 most likely correspond to MC carbides, with M being predominantly Ti, Ta, and W, as reported previously [59,60]. MC carbides, as well as γ' intermetallic precipitates are used to enhance creep resistance at high

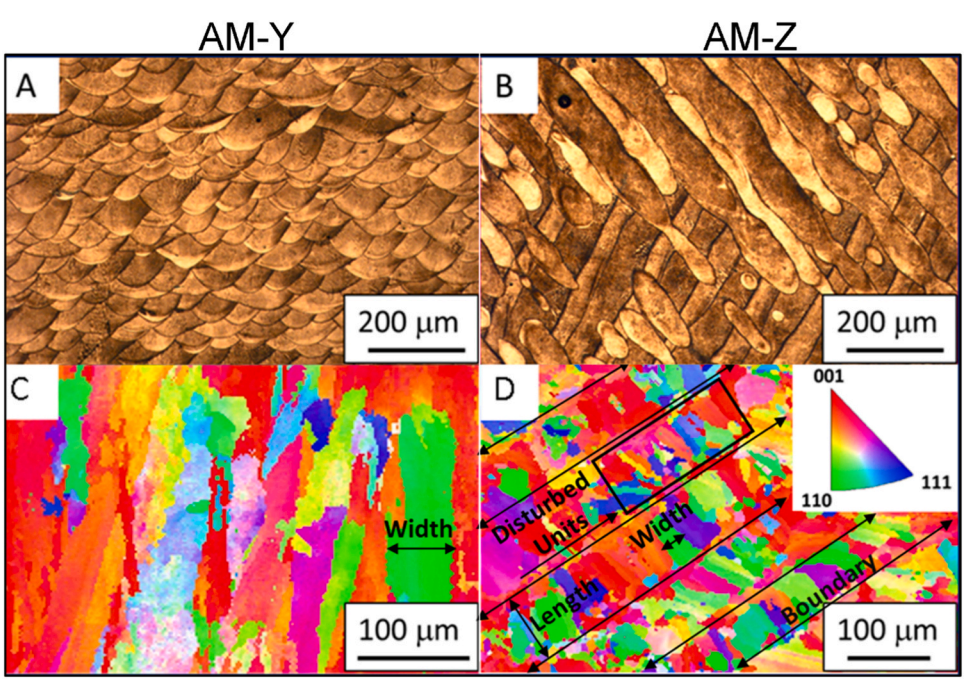

Fig. 1. Optical micrographs and EBSD IPF maps of unexposed IN939 AM-Y (A,C) and AM-Z (B,D).

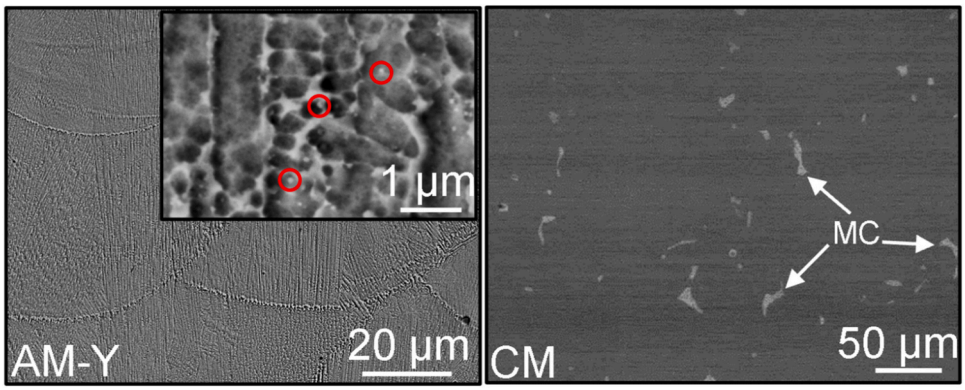

Fig. 2. SEM-BSE images of unexposed AM-Y IN939 and CM IN939. Red circles in the high magnification inset in AM-Y indicates MC carbides.

temperatures [53].

Fig. 3 shows the mass gain values after 168 h of exposure under dry conditions for the different types of IN939 samples. It is clear that there is minimal variation in mass gain between AM-X, AM-Y and AM-Z, indicating that the anisotropic nature of the material has a negligible effect on the oxidation properties. A comparison of the AM IN939 and CM IN939 materials also shows no significant differences. Therefore, the present data confirm that from the oxidation point of view, this new production route is as effective as the CM method. The recorded mass gains of circa 0.8 mg·cm^{-2} are in good agreement with the data reported in the literature. For example, Abedini et al. [61] obtained a value of around 1 mg·cm^{-2} after approximately 1 week of exposure at 930°C. Lee et al. [62] reported a mass gain value of 0.6 mg·cm^{-2} after 75 hours at 870°C. Furthermore, the AM material exhibits some spallation of the oxide scale. However, the surface fraction of spalled regions is relatively small (<1%) and the effect of spallation on the mass gain is estimated to be <0.1 mg·cm^{2}. This will be discussed further below. Nonetheless, longer exposures (>1000 h) are required to fully determine the oxidation behavior of AM IN939 as an alternative material to conventionally produced IN939 for possible high temperature applications.

Fig. 4 depicts the GI-XRD diffractogram of the samples exposed

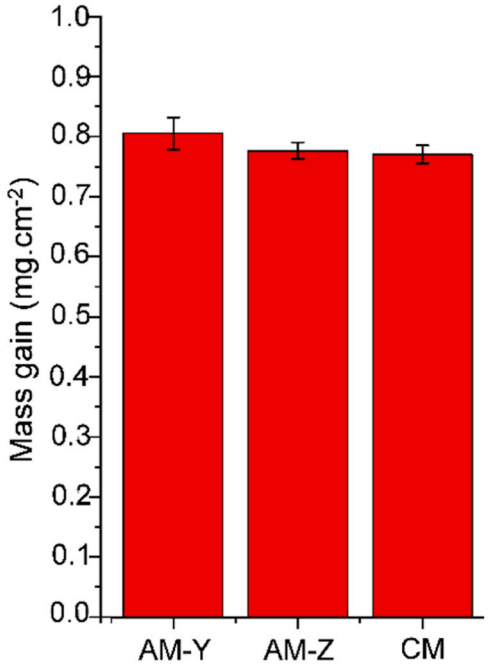

Fig. 3. Mass gain plots for AM-Y, AM-Z, and CM IN939 alloys after 1 week of exposure at 900°C in dry air.

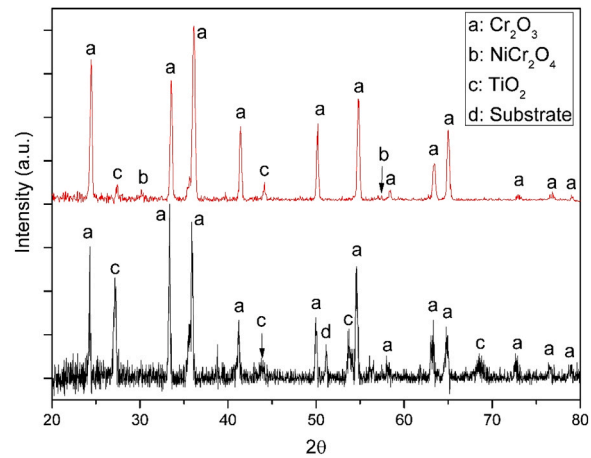

Fig. 4. XRD diffractograms of AM-Y IN939 (in red) and CM IN939 (in black) after 1 week of exposure at 900°C.

under dry conditions. Both the CM and AM samples are covered with Cr_2O_3 (Eskolaite: 01–074–6677), TiO_2 (Rutile: 04–003–0648). Additionally, $NiCr_2O_4$ phase (Nichromite: 00–023–1271) was detected on AM IN939 while peaks belonging to this phase were missing on CM IN939. This behavior is possibly related to the incorporation of Ti into the oxide scale. More will be discussed about this subject in the upcoming sections. Furthermore, no peaks for MC carbides were detected, possibly because, the volume fraction of this phase is below the detection limit of XRD [47].

Fig. 5 shows the plan-view SEM images (Secondary Electron, SE) of the AM, AM-Y, and AM-Z AM IN939 samples and the CM IN939 samples after 168 h of oxidation at 900°C in dry air. Fig. 6 shows the corresponding EDX maps of the same samples. Additional high magnification SEM-EDX mapping analysis are given in Fig. S2. As shown in Fig. 6 and Fig. S2, the surface is covered mostly with O, Cr, Ni and Ti and this pattern matches well with the phase identification made by XRD, which confirms the presence of Cr_2O_3, $NiCr_2O_4$ and TiO_2. Most of the surfaces of the samples are covered with a uniform layer of Cr_2O_3, although minor differences in surface morphology are apparent. On the AM IN939 samples, ridges are randomly distributed on the surface (insets in Fig. 5, A and B), and this indicates thicker oxide formation in localized regions. These ridges likely form above the metal grain boundaries. Furthermore, according to the SEM-EDX maps (Fig. 6, A and B), these ridges are decorated with TiO_2 precipitates. However, ridges are not observed on the CM IN939 samples. This is attributed to the fact that there are very few grain boundaries in CM IN939 due to its very large grain size. The EDX mapping of the AM-Y samples reveals some non-homogeneously dispersed areas that are rich in Ni and Cr, which most probably

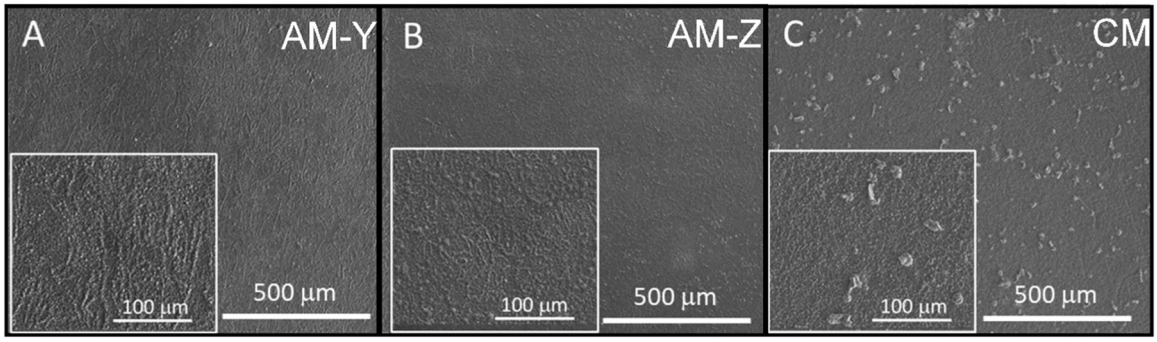

Fig. 5. Plan-view SEM-SE images of AM-Y (A), AM-Z (B), and CM (C) IN939 after 1 week of exposure at 900°C. Each inset is a higher magnification of the same surface.

correspond to Ni-Cr spinel, as reported in previous studies which form during the transient oxidation stage [62]. On CM IN939, Ni enriched regions were also observed but they were rather limited compared to AM IN939 shown by the XRD analysis.

Another notable difference between the AM IN939 and CM IN939 is the presence of isolated large particles on the surface, with an approximate size of 20–100 µm on CM IN939 (Fig. 5C). These particles are rich in Ti, W, Ta, or Nb and are probably the protruding part of oxidized coarse MC carbides that are not present in the AM IN939 materials. This mechanism has been described previously by Litz et al. [63] and will be commented upon below.

Fig. 7 shows the cross-sections (SEM-SE) of the AM-Y, AM-Z, and CM IN939 samples after the exposure. Fig. 8 depicts the SEM-EDX maps for the same set of samples. According to the cross-sectional images, an externally grown Cr_2O_3 layer with an average thickness of 3 µm is present on all the samples. The layer is continuous and homogeneous, and no obvious differences on the externally grown scale between the samples is observed in terms of phase constituents and scale thickness due to microstructural anisotropy. This means that the microstructural anisotropy of the AM material is not affecting the oxidation behavior under these conditions. The obvious difference in the oxide scales is the scale detachment and excessive buckling observed for AM IN939. It should be mentioned that spallation exists in both AM IN939 samples, according to the plan-view SEM investigations (Fig. S3). The reason for having an adherent cross-section in the AM-Y sample is related to the low probability of finding almost-detached and spalled regions using cross-sectional investigations. On the contrary, the CM IN939 is well-adhered, and no buckling of oxide scales is observed. However, pores are formed between the metal and the oxide layer. An internal oxidation zone (IOZ) is present in all the specimens. This IOZ is mostly composed of Al_2O_3, as confirmed by the Al and O maps (Fig. 8). The depth of the IOZ (from Fig. 7 and Fig. 8) reaches 7–8 µm in the AM-Y materials, 3–4 µm in the AM-Z, and 5–6 µm in the CM IN939, which reveals that the inward oxygen diffusion is affected by the anisotropy and the grain size. The size of the precipitates within the IOZ (presumed to be Al_2O_3) are coarser in the AM samples than in the CM samples.

Further into the substrate, mainly at the grain boundaries, at up to 20–30 µm inside the material, an internal nitridation zone (INZ) is present both in AM IN939 and CM IN939 which is in agreement with the findings of Litz et al. [64]. However, based on the SEM-EDS findings, in AM IN939 both Al and Ti formed nitrides while only Ti is being nitrided in CM IN939. This is most probably related with the alloy microstructure and will be discussed more at the end of this section. In the IOZ and INZ, coarse aluminum-rich particles can be observed (oxides on top and nitrides deeper in the alloy). According to a study conducted by Krupp et al. [65], this might be related to the detachment of the Cr_2O_3 scale, which seems to promote N diffusion towards the substrate and result in the nitridation of Al. Litz et al. [63] have proposed a similar mechanism for the nitridation of Ti on IN939. However, the formation of such cracks is not needed for the nitridation of Al and Ti, since Cr_2O_3 scales have been shown to be permeable to N [66–68]. In the INZ of the AM materials, TiN accumulates at the grain boundaries and in the form of small precipitates in the grains themselves, while bulky AlN particles are found at a depth of around 10 µm from the surface. In general, the depth of the INZ is less (14 ± 3 µm) in the CM material than in the AM material (≈20 µm), as can be seen clearly in Fig. 7. Thus, the smaller grain size and cellular/dendritic substructure of the AM material might explain the greater depth of the INZ, promoting N diffusion. The depth of the INZ does not differ significantly between the AM samples, proving that the cutting direction does not influence the permeation of N inside the material. Furthermore, the INZ depth is constant for the AM samples, while in the CM samples, the depth of the INZ varies locally and is somewhat deeper close to the metal grain boundaries, creating a wavy interface (Fig. 7C), which is also related to grain size. Regarding the formation of different nitrides in AM IN939 (AlN, TiN) and CM IN939 (only TiN), TiN is thermodynamically more stable compared to AlN [69]. Thus thermodynamically, TiN is the expected nitride phase to form by internal nitridation. However, as discussed earlier, due to fine dendritic/cellular structure of the as-printed AM IN939 alloy, nitrogen flux is expected to be higher in AM IN939 compared to CM IN939. This is reflected in the depth as well as in the morphology (mimicking the cellular structure of alloy) of internal nitridation zone in Fig. 7. Due to enhanced nitrogen flux in the as-built AM IN939, AlN precipitates formed despite their low stability as an additional nitride phase. On CM IN939, AlN phase is missing since the nitrogen flux is relatively low in that material owing to its large grain size. Moreover, Litz et al. [63,64] also only observed TiN in the INZ who also studied a coarse-grained IN939 produced by casting. Additionally, in the upcoming sections it will be shown that, annealed AM IN939 also only exhibits TiN as the sole nitride compound in the INZ. In addition to the differences in INZ, the AM microstructure was also found to affect the phases formed in the oxide scales; previously it was shown that in AM IN939 peaks belonging to $NiCr_2O_4$ phase were found in the XRD diffractogram while this phase was missing on CM IN939. Instead, TiO_2 peaks were more distinct in CM IN939. Since Ti was mainly bound as TiN in AM IN939 (deeper INZ) less incorporation of Ti was found in the oxide of AM IN939. On the contrary, both shallow INZ and the porous oxide scale of CM IN939 shows that Ti incorporated more in the oxide scale formed on CM IN939 (Fig. 7).

In CM IN939 after the exposure, coarse precipitates (5–30 µm, bright precipitates) are observed in the alloy matrix (Fig. 9). According to the SEM-EDX maps (Fig. 9) the precipitates are rich in Ti, Ta, and Nb and are identified as the aforementioned MC carbides [60,63]. In contrast, in the AM material, these features are not found. Instead, some Cr-rich particles are present (Fig. 9A) deep within the substrate (>25 µm from the surface). It is speculated that these are $M_{23}C_6$ carbides, where M is usually Cr. Other investigators have previously noticed that at temperatures <930°C, the MC carbides tend to disappear with the formation of this new type of carbide, mostly localized in the grain boundaries [46]. The formation of carbides in the grain boundaries might decrease the

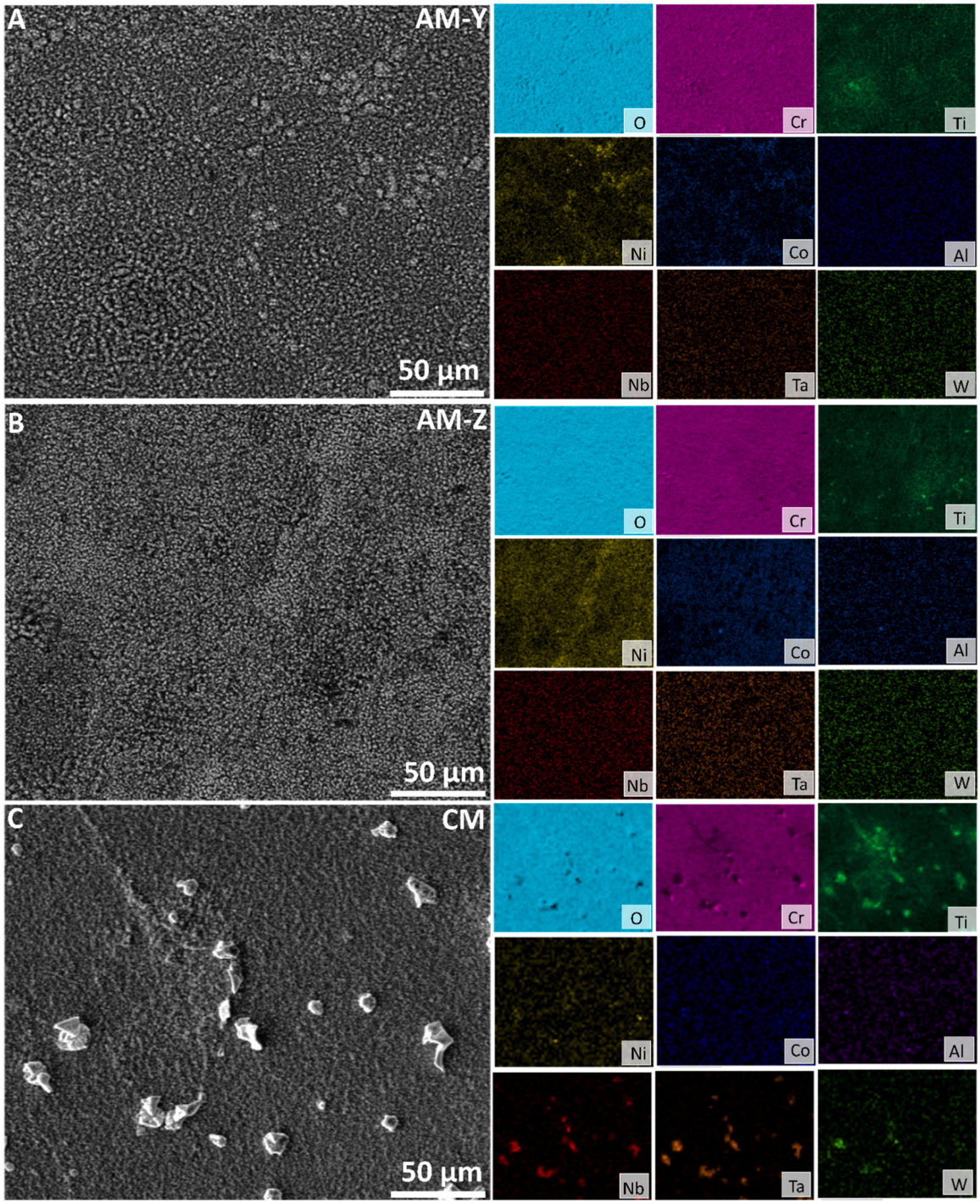

Fig. 6. Plan-view SEM-SE images and related EDX maps of AM-Y (A), AM-Z (B), and CM (C) IN939 after 1 week of exposure at 900°C in laboratory air.

mechanical properties of the alloy during service at high temperatures, so it should be avoided [61,70,71]. In the CM IN939 material, the coarse carbides cause cracking of the oxide scale, which manifest themselves as particles on the surface (see Fig. 6C). This is due to the volume expansion of the carbide that occurs upon oxidation, as discussed by Litz et al. [63]. In the AM material, no outward-growing particles are found on the surface, due to the absence of large MC carbides.

The cross-sectional images (Fig. 8) show tantalum (Ta) enrichment in the AM IN939 material below the Cr_2O_3 scale; this phenomenon is slightly more distinct in the AM sample than in the CM sample. AM IN939 contains more Ta (1.59 wt%) compared to CM IN939 (1.1 wt%). Yet, this is a rather minor difference in composition. However, since Ta is mainly located in MC carbides, the difference in Ta segregation is probably related with the size of the carbides. The carbide size in CM IN939 is very large (on the order of 20 µm) while in the as-built AM IN939, they are much smaller and on the order of ≈100 nm (Fig. 2). Hence, the size difference of carbides in the two materials leads to a surface area difference which probably results in higher dissolution rates in the latter (AM IN939). A similar result is found in [72]. According to that study, coarse chromium carbides ($Cr_{23}C_6$) found in as-cast austenitic Fe-Cr-C alloy were not able to supply enough Cr to the surface while relatively fine carbides found in the hot-forged Fe-Cr-C alloy provided the necessary Cr supply to form and maintain Cr_2O_3 scale during the oxidation [72].

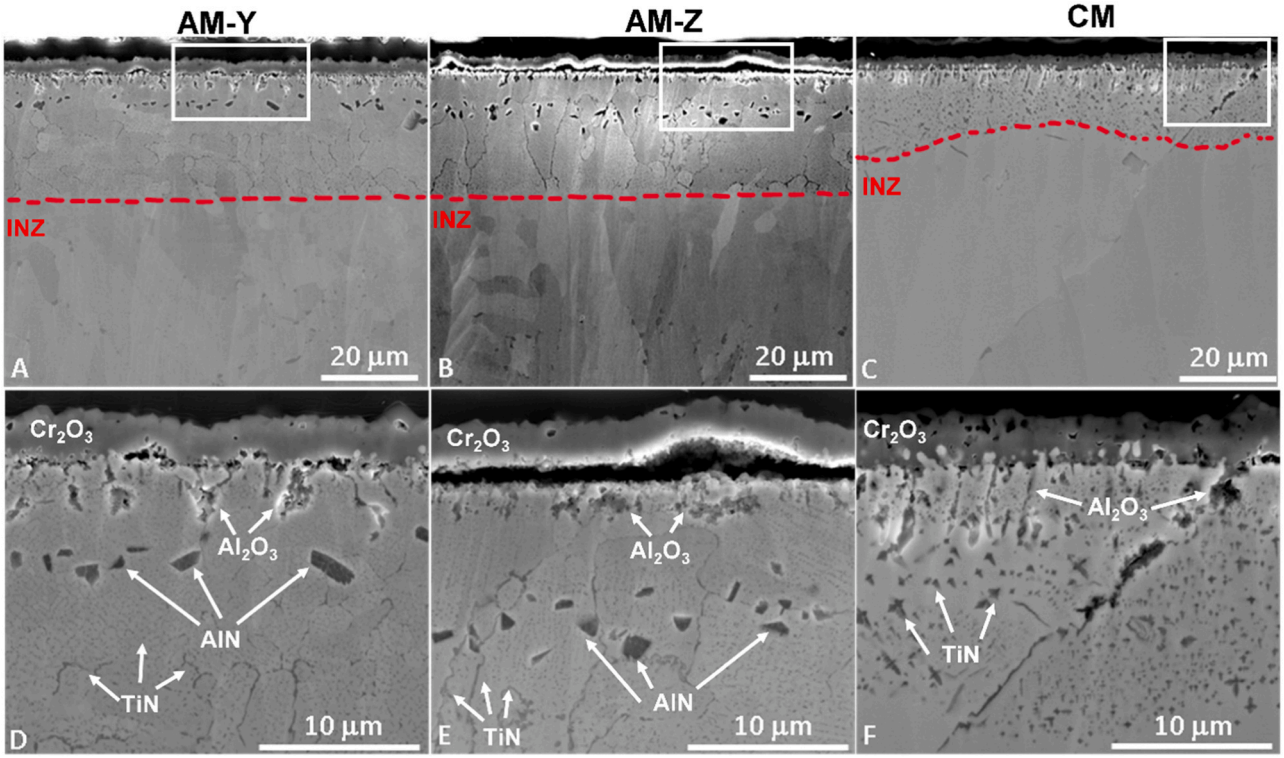

Fig. 7. SEM-SE cross-sectional images and their corresponding magnified images (insets) of: AM-Y (A, D), AM-Z (B, E), and CM (C, F) IN939 after 1 week of exposure at 900°C in laboratory air.

The segregation of Ta below the Cr_2O_3 scale corresponds to the formation of Ta-rich oxides such as TaO_2 and Ta_2O_5, which are more stable than Cr_2O_3 [73,74]. Furthermore, these oxides can react with Cr_2O_3 or TiO_2 to form $CrTaO_4$ and $TiTaO_4$, respectively, depending on the Cr, Ta and Ti concentrations of the alloys [74]. Litz et al. [64] oxidized IN939 at 1100°C for up to 100 h and identified the Ta-enriched layer as $(Ta,Ti,Nb)O_2$. Since the studied alloys are identical (IN939), it seems likely that the Ta-enriched region corresponds to $(Ta,Ti,Nb)O_2$. The effect of the Ta concentration on the high-temperature oxidation behaviors of Cr_2O_3-forming Ni-based alloys have been investigated in several studies [73–80]. According to those studies, the effect of Ta can be both detrimental and beneficial to the high temperature oxidation resistance of these alloys, depending on the concentrations and the synergistic effects of other elements, such as Al and Ti [73,74]. For example, when up to 2 wt% Ta was added to the IN617 alloy the oxidation rates at 900°C and 1000°C were reduced approximately 1.5-fold due to the formation of a TaO_2 sublayer underneath the Cr_2O_3 scale [80]. Gao et al. [80] have claimed this sublayer slows down both the inward diffusion of O and the outward diffusion of Ti. Yet, 1.5 wt% Ta addition has been shown to be detrimental to the oxidation behaviors of ternary Ni-based model alloys (Ni-20Cr-xTa) due to the formation of $CrTaO_4$ and TaO_x, promoting crack and pore formation in the Cr_2O_3/-TaO_x at the metal/oxide interface [73]. Furthermore, Berthod et al. [75–79] have shown that the incorporation of 5–6 wt% Ta into Ni-20Cr alloys is detrimental to oxide adherence due to the formation of the $CrTaO_4$ phase. Whether Ta has a positive or a negative influence on scale adhesion in the present study will be discussed in the upcoming sections.

Another aspect of the AM and CM materials that possibly affects the oxide scale morphology and adhesion are differences in microstructure. As noted above, CM IN939 has coarse grains of up to 500 µm, while AM IN939 in the as-build state possesses rectangular repeating units that are 40–60 µm long and 10–15 µm wide. Furthermore, AM IN939 exhibits a fine dendritic/cellular substructure (Fig. 1, Fig. 2). On fine-grained Cr_2O_3-forming alloys, ridges are commonly found on top of the metal grain boundaries, while flat interfaces are observed on the scales that grow on top of the grains [81–83]. Since the ridges are usually thicker than the adjacent oxide formed on top of the grains, it is likely that they will induce stresses during the growth of the oxide scales (lateral growth), which will contribute to the spallation, as shown in the study of Athreya et al. [81].

To investigate further the effect of microstructure on the high-temperature oxidation properties, an annealing experiment was performed on AM IN939. AM IN939 was annealed at 1160°C for 1 week, followed by an ageing step of 24 hours at 800°C. Thereafter, the annealed samples were exposed under the same conditions (900°C for 168 h). Fig. 10 depicts a wider cross-sectional SEM image of the oxide scale formed after 168 h at 900°C, and Fig. 11 shows the SEM/EDX analysis of the annealed AM IN939 after exposure of the samples at 900°C for 168 h in dry air. Plan-view image of annealed and oxidized AM IN939 is given in Fig. S4. An additional High magnification cross-sectional SEM-BSE image is also given in Fig. S5. Previously, it has been shown that oxide scale-metal adhesion is poor in the as-printed material, as evidenced by the loss of contact between the oxide scale and metal (Fig. 7E), while in CM IN939 alloy, no scale detachment is observed (Fig. 7F). According to Fig. 10, annealed AM IN939 shows an intermediate behavior, with better adherence of the scale to the metal substrate and with no scale buckling (Fig. S4). This shows that an improvement of oxide adherence by heat treatment is achievable and that this is most probably related to the microstructure of the alloy. The larger grain size (≈50 µm) after the annealing process eliminated the wrinkling/buckling of the Cr_2O_3 scale due to the decreased surface area of the grain boundaries. Yet, a local variation of oxidation behavior is evident in the cross-sectional analysis, in that some parts of the sample exhibit poor adhesion, similar to AM IN939 (marked as I in Fig. 10), while other parts have a microstructure that more closely resembles CM IN939 (marked as II in Fig. 10). The better-adhered portions of the scale are more-porous and contain Ti-oxide particles at the gas-oxide interface (see the EDX maps in Fig. 11 and Fig. S6). Furthermore, there is a tendency towards less-deep nitridation of Ti in the well-adhered sections. It seems that Ti is either tied up as nitride (regions with poor adhesion) or

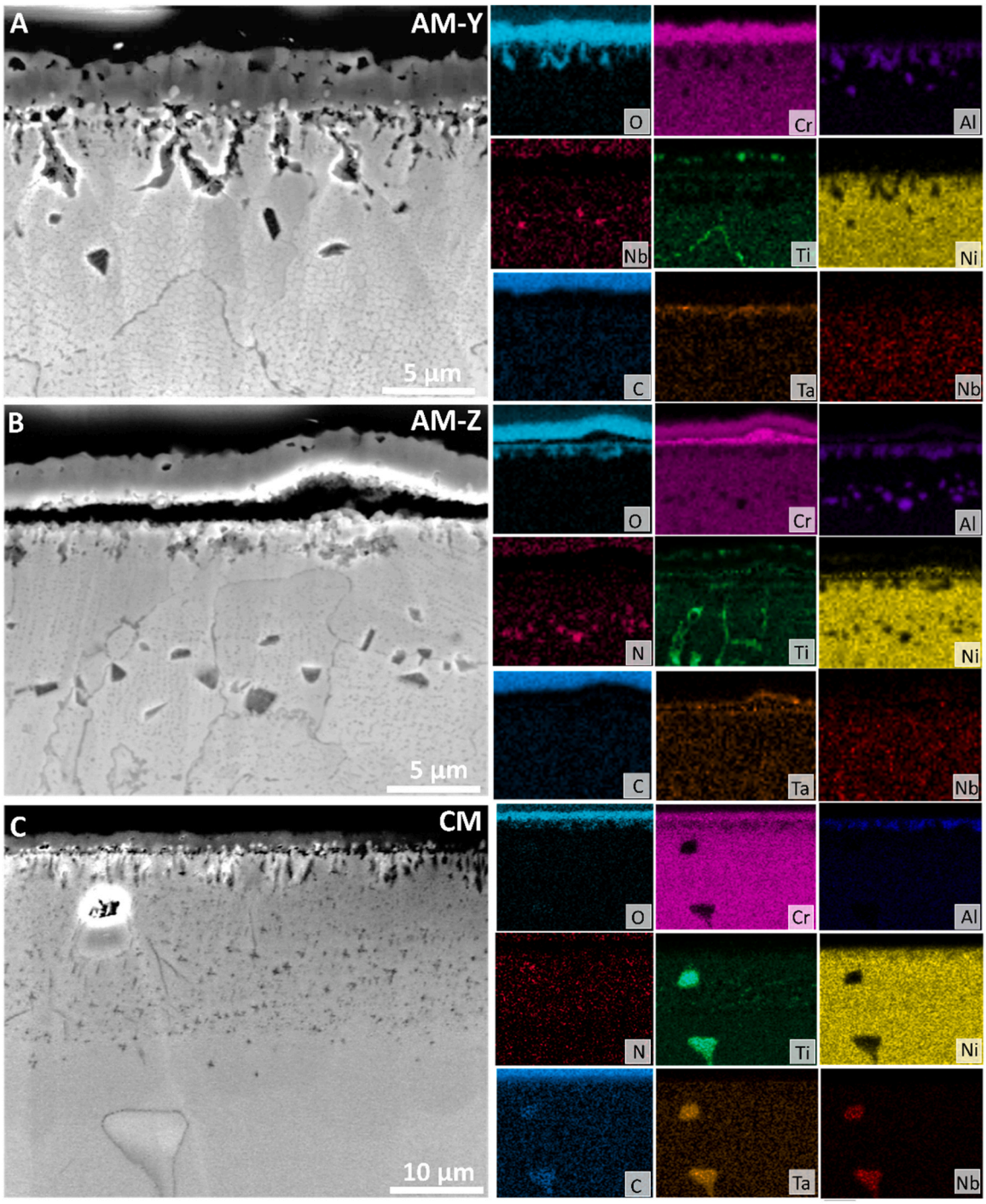

Fig. 8. SEM-SE cross-sectional images and related EDX maps for AM-Y (A), AM-Z (B), and CM (C) IN939 after 1 week of exposure at 900°C in laboratory air.

incorporated into the oxide scale (well-adhered regions). Incorporation of Ti has been shown to modify the oxide structure, resulting in a porous thicker scale and TiO_2 formation at the gas/oxide scale interface [81, 82]. On the annealed AM IN939 sample, the INZ (compared to the as-printed sample) is shallow (12 µm ± 4 µm) and resembles more the CM IN939 sample. This behavior is related to the coarsening of the grains and the disappearance of the fine dendritic/cellular structure, which obviously decelerates the inwards diffusion of N. Replacement of the fine dendritic/cellular structure with coarse grains also affected the formation of phases in the INZ due to decelerated N diffusion. In as-printed AM IN939, both AlN and TiN are found in the INZ while only TiN was found on CM IN939 (Fig. 8). Annealed AM IN939 with its coarse-grained structure also only exhibits TiN in the INZ (Fig. 11). This finding supports the previously discussed effect of the AM microstructure that it not only affects the depth of INZ, but also the formed phases within the INZ.

Another effect that annealing has on the microstructure of AM is reflected in the size of the carbides. In the as-printed condition, the small bright particles (<100 nm) are interpreted as MC carbides (Fig. 2A) and no coarse carbides are found even after the exposures (Fig. 7E). However, in the annealed AM IN939, coarse carbides are clearly visible in Fig. 10 and Fig. 11 as homogenously distributed bright precipitates in the matrix (≈1 µm). Despite exhibiting coarse MC precipitates in the microstructure, Ta enrichment, as an almost continuous layer, is

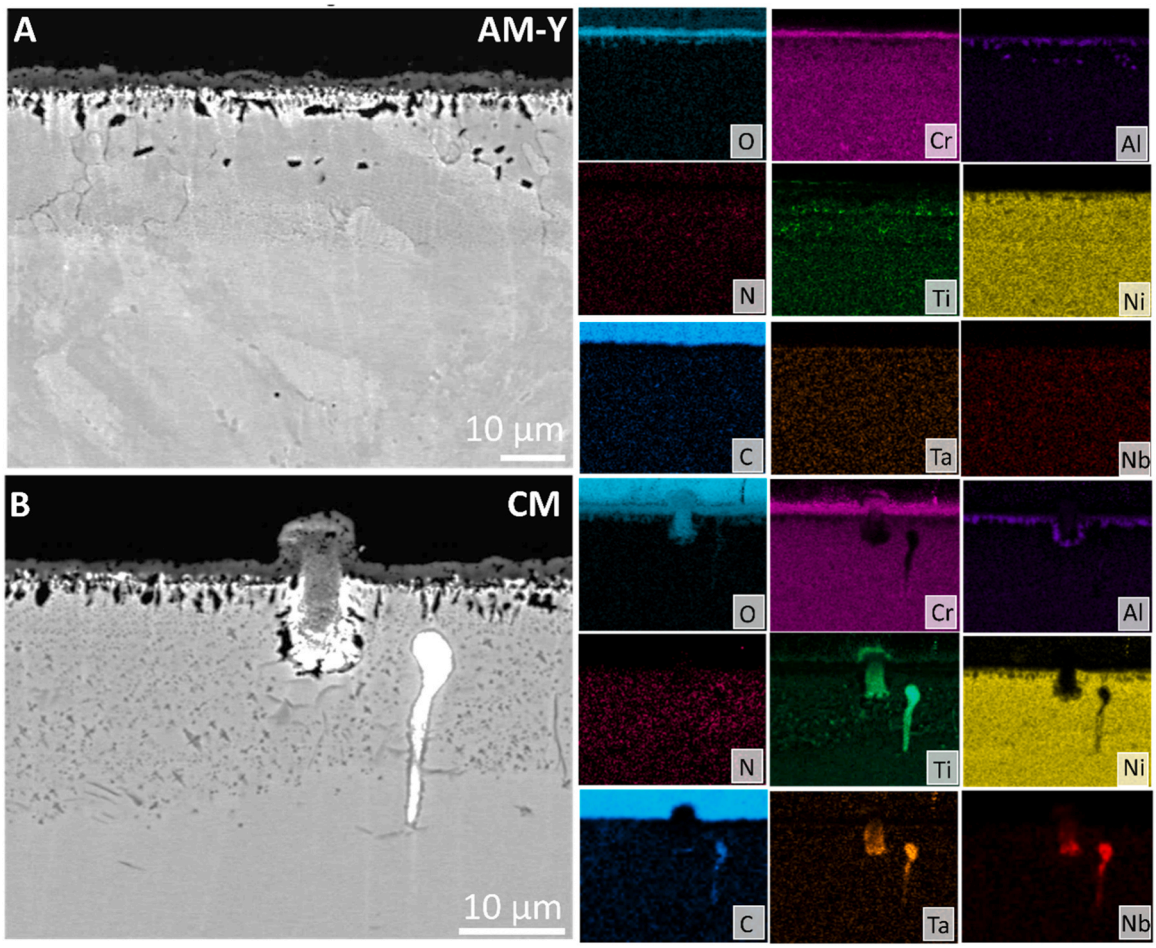

Fig. 9. SEM-BSE cross-sectional images (carbide) and related EDX maps for AM-Y (A) and CM (B) IN939 after 1 week of exposure at 900°C in laboratory air.

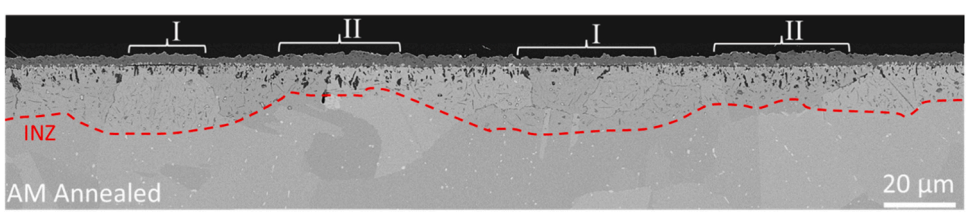

Fig. 10. SEM-BSE cross-sectional image of annealed and oxidized AM IN939 after 1 week of exposure at 900°C in laboratory air. I represents poorly adhered regions with deeper INZ while II represents regions with better adhesion and shallow INZ.

detected in the annealed sample below the Cr_2O_3 scale (Fig. 11). Yet, Ta enrichment does not seem to have any adverse effect on the adherence of Cr_2O_3 layer, since in the well-adhered regions, slightly more Ta enrichment is detected by SEM-EDX analysis (Fig. 11). In fact, in the Ta-rich regions, Al_2O_3 precipitates are found slightly deeper in the metal, while they are located directly at the metal-oxide interface in the regions that have less Ta. It is speculated that the presence of Al_2O_3 at the metal/oxide interface affects the scale adhesion and results in the loss of contact during the cooling stage, for example, due to thermal expansion coefficient difference, while the formation of Al_2O_3 precipitates slightly deeper in the metal does not induce this effect. Therefore, the AM microstructure at least in the as-printed state is found to highly affect the internal nitridation (depth and formed phases within), incorporation of elements (Ti) in the oxidation process and oxide adhesion. Performed annealing at 1160 °C for 1 week mostly eliminated the problems that is encountered on as-built state.

4. Conclusion

This study highlights how AM-produced IN939 exhibits corrosion rates at 900°C that are similar to those for conventionally manufactured (CM) IN939, irrespective of the orientation of the oxidized surface with respect to the building direction. Both materials formed Cr_2O_3 as a protective oxide scale, yet some differences in oxide scale morphology and composition are observed. More Ti is incorporated in the scale of CM IN939. Additionally, the AM IN939 shows some signs of oxide spallation, which are not observed in the CM IN939.

Both materials exhibit an internal oxidation zone (IOZ) and internal nitridation zone (INZ). The IOZ of AM IN939 and CM IN939 are both composed of Al_2O_3. Some Ta enrichment as TaO_x was also observed below the Cr_2O_3 scale. The INZ of as-built AM IN939 consists of AlN and TiN while only TiN is found in the INZ of CM IN939. In AM IN939 the INZ has a rather constant depth and penetrates deeper into the metal compared to CM IN939 where the INZ is more localized at the grain

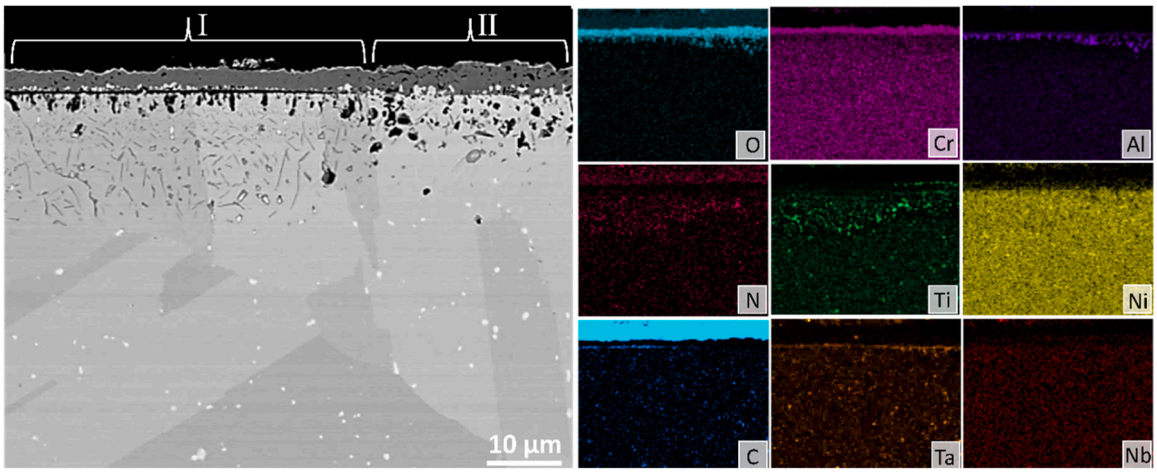

Fig. 11. SEM-BSE cross-sectional image and related EDX maps for annealed and oxidized AM IN939 material after 1 week of exposure in laboratory air at 900°C. I represent poorly adhered regions with deeper INZ while II represents regions with better adhesion and shallow INZ.

boundaries.

It is proposed that, these differences both in oxidation and internal nitridation are related to the smaller grain size with a fine dendritic/cellular structure of as-built AM IN939. It is suggested that, the finer structure in AM IN939 results in more pronounced wrinkling/buckling of the oxide scales. Furthermore, finer structure most probably enhances the inwards nitrogen flux and promotes the formation of AlN along with TiN.

An additional heat treatment improves the oxide scale adhesion of the AM material, attributed the to coarsening of the grains, which eliminates wrinkling of the oxide scales and results in a shallow INZ. Furthermore, the coarsened AM material exhibited a similar INZ as CM IN939.

In addition, on the annealed and oxidized AM IN939 material, there is a local variation of the oxidation properties in terms of scale adhesion, oxide scale thickness, and pore concentration. The thickness and pore concentration of oxide scales seems to correlate with the incorporation of Ti into the scale. The thickness of the INZ on annealed and oxidized AM IN939 also changes locally; regions with deeper INZ have less Ti incorporation into Cr_2O_3 scale while more Ti incorporation is observed on regions with shallow INZ.

Moreover, in the regions with more pronounced Ta enrichment, Al_2O_3 forms not exactly at the metal-oxide interface but deeper within the metal. It is speculated that the presence of Al_2O_3 at the metal/oxide interface might have a negative influence on oxide adhesion.

CRediT authorship contribution statement

Kerem Ozgur Gunduz: Conceptualization, Investigation, Writing – original draft, Writing – review & editing. **Alberto Visibile:** Conceptualization, Investigation, Writing – original draft. **Jan Froitzheim:** Conceptualization, Funding acquisition, Project administration, Writing – original draft, Writing – review & editing. **Mats Halvarsson:** Funding acquisition, Project administration, Writing – review & editing. **Irina Fedorova:** Investigation. **Mohammad Sattari:** Investigation, Writing – review & editing.

Declaration of Competing Interest

The authors declare that they have no known competing financial interests or personal relationships that could have appeared to influence the work reported in this paper.

Data availability

Data will be made available on request.

Acknowledgments

This study was carried out within the Swedish High Temperature Corrosion Centre (HTC) and the authors gratefully acknowledge HTC, together with the Swedish Energy Agency and its Member Companies (Siemens Energy AB, Alleima AB, Kanthal AB). The authors also gratefully acknowledge the Chalmers Materials Analysis Laboratory (CMAL), where the SEM-EDS investigations were carried out. Thanks also to Siemens Energy AB for providing CM IN939.

Appendix A. Supporting information

Supplementary data associated with this article can be found in the online version at doi:10.1016/j.corsci.2024.112067.

References

[1] H. Long, S. Mao, Y. Liu, Z. Zhang, X. Han, Microstructural and compositional design of Ni-based single crystalline superalloys–A review, J. Alloy. Compd. 743 (2018) 203–220.
[2] T.M. Pollock, S. Tin, Nickel-based superalloys for advanced turbine engines: chemistry, microstructure and properties, J. Propuls. Power 22 (2006) 361–374.
[3] S. Utada, L. Despres, J. Cormier, Ultra-high temperature creep of ni-based sx superalloys at 1250C, Met. (Basel) 11 (2021) 1610.
[4] W.H.C. Sims, N. Stoloff, Superalloys II: High. -Temp. Mater. Aerosp. Ind. Power (1987).
[5] M.J. Donachie, Superalloys: A Technical Guide, 2nd Edition, America (NY), 2002, pp. 1–409, https://doi.org/10.1361.
[6] R.C. Reed, Superalloy fundamentals and applications, 2006.
[7] G.B. Schaffer, S.H. Huo, J. Drennan, G.J. Auchterlonie, The effect of trace elements on the sintering of an Al-Zn-Mg-Cu alloy, Acta Mater. 49 (2001) 2671–2678, https://doi.org/10.1016/S1359-6454(01)00177-X.
[8] M. Moattari, M.M. Shokrieh, H. Moshayedi, H. Kazempour-Liasi, Evaluations of residual stresses in repair welding of Ni-based IN939 superalloy, J. Therm. Stress. 43 (2020) 801–815, https://doi.org/10.1080/01495739.2020.1751759.
[9] M. Abedini, M.R. Jahangiri, P. Karimi, Rejuvenation of the microstructure and mechanical properties of a service-exposed IN939 superalloy by heat treatments, Mater. High. Temp. 36 (2019) 19–26, https://doi.org/10.1080/09603409.2018.1448529.
[10] G. Sjöberg, D. Imamovic, J. Gabel, O. Caballero, J.W. Brooks, J.P. Ferté, A. Lugan, Evaluation of the IN 939 alloy for large aircraft engine structures, Proc. Int. Symp. Superalloys. (2004) 441–450. https://doi.org/10.7449/2004/superalloys_2004_441_450.
[11] J.J. Schirra, C.A. Borg, R.W. Hatala, Mechanical property and microstructural characterization of vacuum die cast superalloy materials, Proc. Int. Symp. Superalloys (2004) 553–561, https://doi.org/10.7449/2004/superalloys_2004_553_561.

[12] R. Couturier, C. Escaravage, High temperature alloys for the htgr gas turbine: required properties and development needs, Gas. Turbine Power Convers. Syst. Modul. HTGRs. Rep. a Tech. Comm. Meet. (2001) 163–176.
[13] T. DebRoy, H.L. Wei, J.S. Zuback, T. Mukherjee, J.W. Elmer, J.O. Milewski, A. M. Beese, A. Wilson-Heid, A. De, W. Zhang, Additive manufacturing of metallic components – Process, structure and properties, Prog. Mater. Sci. 92 (2018) 112–224, https://doi.org/10.1016/j.pmatsci.2017.10.001.
[14] W.E. Frazier, Metal additive manufacturing: a review, J. Mater. Eng. Perform. 23 (2014) 1917–1928, https://doi.org/10.1007/s11665-014-0958-z.
[15] A.A. Shapiro, J.P. Borgonia, Q.N. Chen, R.P. Dillon, B. McEnerney, R. Polit-Casillas, L. Soloway, Additive manufacturing for aerospace flight applications, J. Spacecr. Rockets 53 (2016) 952–959, https://doi.org/10.2514/1.A33544.
[16] Y. Kok, X.P. Tan, P. Wang, M.L.S. Nai, N.H. Loh, E. Liu, S.B. Tor, Anisotropy and heterogeneity of microstructure and mechanical properties in metal additive manufacturing: a critical review, Mater. Des. 139 (2018) 565–586, https://doi.org/10.1016/j.matdes.2017.11.021.
[17] L. Hitzler, J. Hirsch, B. Heine, M. Merkel, W. Hall, A. Öchsner, On the anisotropic mechanical properties of selective laser-melted stainless steel, Mater. (Basel) 10 (2017), https://doi.org/10.3390/ma10101136.
[18] H. KYOGOKU, T.-T. IKESHOJI, A review of metal additive manufacturing technologies: mechanism of defects formation and simulation of melting and solidification phenomena in laser powder bed fusion process, Mech. Eng. Rev. 7 (2020) 19-00182–19–00182, https://doi.org/10.1299/mer.19-00182.
[19] W.J. Sames, F.A. List, S. Pannala, R.R. Dehoff, S.S. Babu, The metallurgy and processing science of metal additive manufacturing, Int. Mater. Rev. 61 (2016) 315–360, https://doi.org/10.1080/09506608.2015.1116649.
[20] P. Platek, J. Sienkiewicz, J. Janiszewski, F. Jiang, Investigations on mechanical properties of lattice structures with different values of relative density made from 316L by selective laser melting (SLM), Mater. (Basel) 13 (2020), https://doi.org/10.3390/ma13092204.
[21] M. Ni, C. Chen, X. Wang, P. Wang, R. Li, X. Zhang, K. Zhou, Anisotropic tensile behavior of in situ precipitation strengthened Inconel 718 fabricated by additive manufacturing, Mater. Sci. Eng. A. 701 (2017) 344–351, https://doi.org/10.1016/j.msea.2017.06.098.
[22] B.S.I. Gibson, D. Rosen, Additive manufacturing technologies, 3D Print., Rapid Prototyp., Direct Digit. Manuf. (2015).
[23] R.J. Hebert, Viewpoint: metallurgical aspects of powder bed metal additive manufacturing, J. Mater. Sci. 51 (2016) 1165–1175, https://doi.org/10.1007/s10853-015-9479-x.
[24] K.N. Amato, S.M. Gaytan, L.E. Murr, E. Martinez, P.W. Shindo, J. Hernandez, S. Collins, F. Medina, Microstructures and mechanical behavior of Inconel 718 fabricated by selective laser melting, Acta Mater. 60 (2012) 2229–2239, https://doi.org/10.1016/j.actamat.2011.12.032.
[25] K. Wang, D. Du, G. Liu, Z. Pu, B. Chang, J. Ju, A study on the additive manufacturing of a high chromium Nickel-based superalloy by extreme high-speed laser metal deposition, Opt. Laser Technol. 133 (2021) 106504, https://doi.org/10.1016/j.optlastec.2020.106504.
[26] A.K. Maurya, A. Kumar, The Impact of Building Orientation on Microhardness and Surface Roughness of Direct Metal Laser Sintered Inconel Alloy, in: V.R. Kalamkar, K. Monkova (Eds.), Adv. Mech. Eng., Springer Singapore, Singapore, 2021, pp. 619–628.
[27] J.J. Lewandowski, M. Seifi, Metal additive manufacturing: a review of mechanical properties, Annu. Rev. Mater. Res. 46 (2016) 151–186, https://doi.org/10.1146/annurev-matsci-070115-032024.
[28] M.R. Condruz, G. Matache, A. Paraschiv, T.F. Frigioescu, T. Badea, Microstructural and tensile properties anisotropy of selective laser melting manufactured IN 625, Mater. (Basel) 13 (2020), https://doi.org/10.3390/ma13214829.
[29] G. Marchese, S. Parizia, A. Saboori, D. Manfredi, M. Lombardi, P. Fino, D. Ugues, S. Biamino, The Influence of the Process Parameters on the Densification and Microstructure Development of Laser Powder Bed Fused Inconel 939, Met. (Basel) 10 (2020), https://doi.org/10.3390/met10070882.
[30] S. Banoth, C.W. Li, Y. Hiratsuka, K. Kakehi, The effect of recrystallization on creep properties of alloy in939 fabricated by selective laser melting process, Met. (Basel) 10 (2020), https://doi.org/10.3390/met10081016.
[31] O.C. Ozaner, Ş. Karabulut, M. İzciler, Study of the surface integrity and mechanical properties of turbine blade fir trees manufactured in Inconel 939 using laser powder bed fusion, J. Manuf. Process 79 (2022) 47–59, https://doi.org/10.1016/j.jmapro.2022.04.054.
[32] A.S. Shaikh, M. Rashidi, K. Minet-Lallemand, E. Hryha, On as-built microstructure and necessity of solution treatment in additively manufactured Inconel 939, Powder Met. (2022), https://doi.org/10.1080/00325899.2022.2041787.
[33] A. Nyhlén, M. Kinell, K.J. Nogenmyr, Experimental investigation of the thermal performance in additively manufactured mini channels, : J. Phys. Conf. Ser. (2021), https://doi.org/10.1088/1742-6596/2116/1/012032.
[34] W. Philpott, M.A.E. Jepson, R.C. Thomson, Comparison of the effects of a conventional heat treatment between cast and selective laser melted IN939 alloy, : Adv. Mater. Technol. Foss. Power Plants - Proc. 8th Int. Conf. (2016).
[35] Y.T. Tang, C. Panwisawas, J.N. Ghoussoub, Y. Gong, J.W.G. Clark, A.A.N. Németh, D.G. McCartney, R.C. Reed, Alloys-by-design: application to new superalloys for additive manufacturing, Acta Mater. 202 (2021), https://doi.org/10.1016/j.actamat.2020.09.023.
[36] C. Juillet, A. Oudriss, J. Balmain, X. Feaugas, F. Pedraza, Characterization and oxidation resistance of additive manufactured and forged IN718 Ni-based superalloys, Corros. Sci. 142 (2018) 266–276, https://doi.org/10.1016/j.corsci.2018.07.032.
[37] T. Sanviemvongsak, D. Monceau, B. Macquaire, High temperature oxidation of IN 718 manufactured by laser beam melting and electron beam melting: Effect of surface topography, Corros. Sci. 141 (2018) 127–145, https://doi.org/10.1016/j.corsci.2018.07.005.
[38] S. Parizia, G. Marchese, M. Rashidi, M. Lorusso, E. Hryha, D. Manfredi, S. Biamino, Effect of heat treatment on microstructure and oxidation properties of Inconel 625 processed by LPBF, J. Alloy. Compd. 846 (2020) 156418, https://doi.org/10.1016/j.jallcom.2020.156418.
[39] E.R. Lewis, M.P. Taylor, B. Attard, N. Cruchley, A.P.C. Morrison, M.M. Attallah, S. Cruchley, Microstructural characterisation and high-temperature oxidation of laser powder bed fusion processed Inconel 625, Mater. Lett. 311 (2022) 131582, https://doi.org/10.1016/j.matlet.2021.131582.
[40] T. Sanviemvongsak, D. Monceau, C. Desgranges, B. Macquaire, Intergranular oxidation of Ni-base alloy 718 with a focus on additive manufacturing, Corros. Sci. 170 (2020) 108684, https://doi.org/10.1016/j.corsci.2020.108684.
[41] N. Ramenatte, A. Vernouillet, S. Mathieu, A. Vande Put, M. Vilasi, D. Monceau, A comparison of the high-temperature oxidation behaviour of conventional wrought and laser beam melted Inconel 625, Corros. Sci. 164 (2020), https://doi.org/10.1016/j.corsci.2019.108347.
[42] A. Chyrkin, K.O. Gunduz, I. Fedorova, M. Sattari, A. Visibile, M. Halvarsson, J. Froitzheim, K. Stiller, High-temperature oxidation behavior of additively manufactured IN625: effect of microstructure and grain size, Corros. Sci. 205 (2022) 110382, https://doi.org/10.1016/j.corsci.2022.110382.
[43] A. Chyrkin, W.J. Nowak, K.O. Gunduz, I. Fedorova, M. Sattari, J. Froitzheim, M. Halvarsson, K.M. Stiller, Intergranular oxidation of additively manufactured Ni-base alloy 625: The role of Si, Corros. Sci. 219 (2023), https://doi.org/10.1016/j.corsci.2023.111234.
[44] K.-S. Kim, S. Yang, M.-S. Kim, K.-A. Lee, Effect of post heat-treatment on the microstructure and high-temperature oxidation behavior of precipitation hardened IN738LC superalloy fabricated by selective laser melting, J. Mater. Sci. Technol. 76 (2021) 95–103, https://doi.org/10.1016/j.jmst.2020.11.013.
[45] J.N. Ghoussoub, S. Utada, F. Pedraza, W.J.B. Dick-Cleland, Y.T. Tang, R.C. Reed, Alloy Design for Additive Manufacturing: early-stage oxidation of nickel-based superalloys, Metall. Mater. Trans. A Phys. Metall. Mater. Sci. (2022), https://doi.org/10.1007/s11661-022-06860-6.
[46] M.R. Jahangiri, M. Abedini, Effect of long time service exposure on microstructure and mechanical properties of gas turbine vanes made of IN939 alloy, Mater. Des. 64 (2014) 588–600, https://doi.org/10.1016/j.matdes.2014.08.035.
[47] Z. Mišković, M. Jovanović, M. Gligić, B. Lukić, Microstructural investigation of IN 939 superalloy, Vacuum 43 (1992) 709–711, https://doi.org/10.1016/0042-207X(92)90115-D.
[48] R. Jiang, M. Li, Y. Yao, J. Guan, H. Lu, Application of BIB polishing technology in cross-section preparation of porous, layered and powder materials: a review, Front. Mater. Sci. 13 (2019) 107–125, https://doi.org/10.1007/s11706-019-0457-0.
[49] T. Wang, Y.Y. Zhu, S.Q. Zhang, H.B. Tang, H.M. Wang, Grain morphology evolution behavior of titanium alloy components during laser melting deposition additive manufacturing, J. Alloy. Compd. 632 (2015) 505–513, https://doi.org/10.1016/j.jallcom.2015.01.256.
[50] A. Zinoviev, O. Zinovieva, V. Ploshikhin, V. Romanova, R. Balokhonov, Evolution of grain structure during laser additive manufacturing. Simulation by a cellular automata method, Mater. Des. 106 (2016) 321–329, https://doi.org/10.1016/j.matdes.2016.05.125.
[51] K. Antony, N. Arivazhagan, Studies on energy penetration and marangoni effect during laser melting process, J. Eng. Sci. Technol. 10 (2015) 509–525.
[52] J. Sieniawski, W. Ziaja, K. Kubiak, M. Motyk, Microstructure and mechanical properties of high strength two-phase titanium alloys, : Titan. Alloy. - Adv. Prop. Control (2013), https://doi.org/10.5772/56197.
[53] P. Kanagarajah, F. Brenne, T. Niendorf, H.J. Maier, Inconel 939 processed by selective laser melting: Effect of microstructure and temperature on the mechanical properties under static and cyclic loading, Mater. Sci. Eng. A. 588 (2013) 188–195, https://doi.org/10.1016/j.msea.2013.09.025.
[54] A. De Luca, C. Kenel, S. Griffiths, S.S. Joglekar, C. Leinenbach, D.C. Dunand, Microstructure and defects in a Ni-Cr-Al-Ti γ/γ' model superalloy processed by laser powder bed fusion, Mater. Des. 201 (2021) 109531, https://doi.org/10.1016/j.matdes.2021.109531.
[55] Y.T. Tang, J.N. Ghoussoub, C. Panwisawas, D.M. Collins, S. Amirkhanlou, J.W. G. Clark, A.A.N. Németh, D. Graham McCartney, R.C. Reed, The effect of heat treatment on tensile yielding response of the new superalloy ABD-900AM for additive manufacturing, Miner. Met. Mater. Ser. (2020), https://doi.org/10.1007/978-3-030-51834-9_103.
[56] I. Šulák, T. Babinský, A. Chlupová, A. Milovanović, L. Náhlík, Effect of building direction and heat treatment on mechanical properties of Inconel 939 prepared by additive manufacturing, J. Mech. Sci. Technol. (2022), https://doi.org/10.1007/s12206-022-2101-7.
[57] E. Nandha Kumar, K.S. Athira, S. Chatterjee, D. Srinivasan, Effect of Heat Treatment on Structure and Properties of Laser Powder Bed Fusion Inconel 939, in: 2022. https://doi.org/10.1115/iam2022-93945.
[58] A.S. Shaikh, Dev. a γ' Precip. Hardening Ni-Base Superalloy Addit. Manuf., Thesis (2018).
[59] A. Formenti, A. Eliasson, H. Fredriksson, On the dendritic growth and microsegregation in Ni-base superalloys In718, In625 and In939, High. Temp. Mater. Process. 24 (2005) 221–238, https://doi.org/10.1515/HTMP.2005.24.4.221.
[60] A. Formenti, A. Eliasson, A. Mitchell, H. Fredriksson, Solidification sequence and carbide precipitation in Ni-base superalloys IN718, IN625 and IN939, High. Temp.

Mater. Process. 24 (2005) 239–258, https://doi.org/10.1515/HTMP.2005.24.4.239.
[61] M. Abedini, M.R. Jahangiri, P. Karimi, Oxidation and hot corrosion behaviors of service-exposed and heat-treated gas turbine vanes made of IN939 Alloy, Oxid. Met. 90 (2018) 469–484, https://doi.org/10.1007/s11085-018-9847-4.
[62] K.N. Lee, C.A. Barrett, J. Smith, Long-term cyclic oxidation behavior of uncoated and coated RE108 and IN939 at 980 and 870°C, J. Therm. Spray. Technol. 9 (2000) 121–127, https://doi.org/10.1361/105996300770350159.
[63] J. Litz, A. Rahmel, M. Schorr, Selective carbide oxidation and internal nitridation of the Ni-base superalloys IN 738 LC and IN 939 in air, Oxid. Met. 30 (1988) 95–105, https://doi.org/10.1007/BF00656646.
[64] J. Litz, A. Rahmel, M. Schorr, J. Weiss, Scale formation on the Ni-base superalloys IN 939 and IN 738 LC, Oxid. Met. 32 (1989) 167–184, https://doi.org/10.1007/BF00664797.
[65] U. Krupp, H.J. Christ, Selective oxidation and internal nitridation during high-temperature exposure of single-crystalline nickel-base superalloys, Metall. Mater. Trans. A Phys. Metall. Mater. Sci. 31 (2000), https://doi.org/10.1007/s11661-000-0051-0.
[66] K. Taneichi, T. Narushima, Y. Iguchi, C. Ouchi, Oxidation or nitridation behavior of pure chromium and chromium alloys containing 10 mass%Ni or Fe in Atmospheric Heating, Mater. Trans. 47 (2006) 2540–2546, https://doi.org/10.2320/matertrans.47.2540.
[67] T. Sand, S. Bigdeli, M. Sattari, J. Andersson, M. Hättestrand, T. Helander, J. Eklund, J.-E. Svensson, M. Halvarsson, L.-G. Johansson, Efficacy of an external chromia layer in reducing nitridation of high temperature alloys, Corros. Sci. 197 (2022) 110050, https://doi.org/10.1016/j.corsci.2021.110050.
[68] C. Geers, V. Babic, N. Mortazavi, M. Halvarsson, B. Jönsson, L.-G. Johansson, I. Panas, J.-E. Svensson, Properties of Alumina/Chromia Scales in N2-Containing low oxygen activity environment investigated by experiment and theory, Oxid. Met. 87 (2017) 321–332, https://doi.org/10.1007/s11085-016-9703-3.
[69] L. Zhu, C. Feng, S. Zhu, F. Wang, J. Yuan, P. Wang, Comparison of CrN, AlN and TiN Diffusion Barriers on the Interdiffusion and Oxidation Behaviors of Ni+CrAlYSiN Nanocomposite Coatings, Crystals 11 (2021), https://doi.org/10.3390/cryst11111333.
[70] M. Aghaie-Khafri, M. Hajjavady, The effect of thermal exposure on the properties of a Ni-base superalloy, Mater. Sci. Eng. A. 487 (2008) 388–393, https://doi.org/10.1016/j.msea.2007.11.010.
[71] S. Xu, J.I. Dickson, A.K. Koul, Grain growth and carbide precipitation in superalloy, UDIMET 520, Metall. Mater. Trans. A Phys. Metall. Mater. Sci. 29 (1998) 2687–2695, https://doi.org/10.1007/s11661-998-0309-5.
[72] R.N. Durham, B. Gleeson, D.J. Young, Factors affecting chromium carbide precipitate dissolution during alloy, Oxid. Oxid. Met. 50 (1998), https://doi.org/10.1023/a:1018880019395.
[73] H. Wang, J. Guo, S. Lei, W. Li, X. Zhang, Unveiling the formation of oxide layers on Ni-16Cr and Ni-20Cr alloys by the addition of Ta, J. Alloy. Compd. 965 (2023) 171361, https://doi.org/10.1016/j.jallcom.2023.171361.
[74] A. Jalowicka, W. Nowak, D. Naumenko, L. Singheiser, W.J. Quadakkers, Effect of nickel base superalloy composition on oxidation resistance in SO 2 containing, high p O 2 environments, Mater. Corros. 65 (2014) 178–187.
[75] P. Berthod, C. Vébert, L. Aranda, Effect of dendritic orientation on the high temperature oxidation kinetic of tantalum-containing nickel-base alloys, J. Mater. Sci. 42 (2007) 352–362, https://doi.org/10.1007/s10853-006-1033-4.
[76] P. Berthod, High temperature properties of several chromium-containing Co-based alloys reinforced by different types of MC carbides (M = Ta, Nb, Hf and/or Zr), J. Alloy. Compd. 481 (2009) 746–754, https://doi.org/10.1016/j.jallcom.2009.03.091.
[77] P. Berthod, J.P. Gomis, G. Medjahdi, P.J. Panteix, L. Aranda, A study of the dependence on the Co and Ni proportions of the oxidation at elevated temperature of TaC-strengthened {Ni and Co}-based cast superalloys, Mater. Chem. Phys. 251 (2020) 123088, https://doi.org/10.1016/j.matchemphys.2020.123088.
[78] P. Berthod, Y. Hamini, L. Aranda, Influence of tantalum on the rates of high temperature oxidation and chromia volatilization for cast (Fe and/or Ni)-30Cr-0.4C alloys, Mater. Sci. Forum 595-598 (PA) (2008) 861–870, https://doi.org/10.4028/www.scientific.net/msf.595-598.861.
[79] P. Berthod, Z. Himeur, Dependence on the chromium content of the high-temperature oxidation behavior of ta-rich nickel-based cast alloys, Oxid. Met. 90 (2018) 135–151, https://doi.org/10.1007/s11085-017-9828-z.
[80] S. Gao, B. He, L. Zhou, J. Hou, Effects of Ta on the high temperature oxidation behavior of IN617 alloy in air, Corros. Sci. 170 (2020) 108682, https://doi.org/10.1016/j.corsci.2020.108682.
[81] C.N. Athreya, K. Deepak, D.I. Kim, B. de Boer, S. Mandal, V. Subramanya Sarma, Role of grain boundary engineered microstructure on high temperature steam oxidation behaviour of Ni based superalloy alloy 617, J. Alloy. Compd. 778 (2019), https://doi.org/10.1016/j.jallcom.2018.11.137.
[82] J.H. Chen, P.M. Rogers, J.A. Little, Oxidation behavior of several chromia-forming commercial nickel-base superalloys, Oxid. Met. 47 (1997), https://doi.org/10.1007/BF02134783.
[83] R.K. Singh Raman, J.B. Gnanamoorthy, Influence of prior-austenite grain size on the oxidation behavior of 9 wt% cr-1 wt% Mo steel, Oxid. Met. 38 (1992), https://doi.org/10.1007/BF00665665.